Diffusion of water into purged volumes

Lubos Brieda[a], John Newcome[b], and Therese Errigo[c]

[a]*Particle In Cell Consulting LLC, Falls Church, VA*
[b]*ASRC Federal, Beltsville, MD*
[c]*NASA Goddard Space Flight Center, Goddard, MD*

ABSTRACT

In this paper, we report on an experimental and numerical effort to characterize removal and infiltration of atmospheric water vapor into a cavity purged with dry GN2. Multiple miniature sensors were used to track humidity and pressure inside a cylindrical enclosure with internal obstruction and a secondary volume. These measurements were compared against the well-known model of Scialdone. Although our data indicate a similar exponential-like decay, the fit parameters differed from the predicted values. In addition, a numerical model was developed to study the purge and infiltration problem in more detail. The model utilizes an Advection-Diffusion solver for the contaminant species, and an incompressible Navier-Stokes solver for the flow velocity. Comparison of preliminary numerical results with the experimental data is presented.

Keywords: purge, water infiltration, molecular contamination, diffusion

1. INTRODUCTION

In his 1978 and 1999 papers, Scialdone[1,2] presented a simple analytical model for estimating the partial pressure of contaminants within a purged cavity. It should be noted that additional models for contaminant infiltration also exist, including the work of Woronowicz.[3] However, the model of Scialdone is one of the one most widely used by the industry, and as such, is the focus of this paper. Scialdone derives the partial pressure of the contaminant from mass conservation,

$$V\frac{dP}{dt} = C(P_0 - P) - Q(P - P_u) \tag{1}$$

Here P is the partial pressure of the contaminant within the cavity, P_0 is the ambient partial pressure of the contaminant, and P_u is the partial pressure of the contaminant within the purge flow. The C and Q coefficients are the diffusive flow rate through the aperture and the volumetric flow rate of the purge gas, respectively. Scialdone does not go into this detail, but this equation can also be derived from the more familiar form of mass conservation found in fluid dynamics, $\partial\rho/\partial t + \nabla\cdot(\rho\vec{u}) = 0$. If we assume isothermal environment and constant volume, the mass conservation equation be rewritten utilizing the ideal gas law $P = \rho RT$ and the divergence theorem to yield

$$V\frac{dP}{dt} = (PuA)_{inlet} - (PuA)_{outlet}$$

The uA term has units of volume per time: this is the volumetric flow rate given by the C and Q terms in the original equation. In the model, $(PuA)_{inlet} = CP_0 + QP_u$, the rate with which the contaminant enters the cavity due to diffusion of ambient environment through the vent, and due to introduction from the purge gas. The outlet flow is given by $(PuA)_{outlet} = CP + QP$. The first term corresponds to the diffusive counterpart to the CP_0 influx term. The QP component is the power carried out by the purge flow.

Equation 1 can be integrated using the integration factor to yield

$$P = k\exp\left(-\frac{C+Q}{V}t\right) + \frac{CP_0 + QP_u}{C+Q} \tag{2}$$

LB: GOES-R & MMS Contamination Control Engineer, e-mail: lubos.brieda@particleincell.com
JN: GOES-R Mechanical Engineering Co-op, TE: MMS Contamination Control Engineer

where the constant k is determined from $P(0) = P_i$ to yield

$$P = \left[\frac{C(P_i - P_0) + Q(P_i - P_u)}{C + Q}\right] \exp\left(-\frac{C + Q}{V}t\right) + \frac{CP_0 + QP_u}{C + Q} \tag{3}$$

The beauty of the above equation is that it governs the entire purge and infiltration behavior. For instance, if $Q = 0$ (no purge flow), Equation 3 reduces to $P = (P_i - P_0)\exp(-(C/V)t) + P_0$, a simple exponential decay or growth from the initial partial pressure P_i to the ambient partial pressure P_0. We can also note that in the steady state limit $t \to \infty$, $P \to (CP_0 + QP_u)/(C + Q)$ and if the purge gas is assumed to be clean ($P_u = 0$), the limiting contaminant partial pressure will be given by

$$P = \frac{P_0}{1 + Q/C} \tag{4}$$

The model however also raises number of questions. These include:

- **Geometry Detail**: the model is effectively 0D, and does not take into account details of the enclosure geometry, besides its volume. The model assumes uniform distribution of the contaminant within the enclosure. Due to the presence of corners, baffles, and other complex geometry, it would be expected that the enclosure will contain regions more difficult to purge than others.
- **Total Pressure**: the model does not take into account the total pressure, or any possible pressure gradient between the internal and external environments. A pressure gradient will result in formation of a finite flow through the aperture, and the ambient infiltration no longer governed by diffusion alone.
- **Aperture Conductance**: Scialdone presented a model for C/V, the normalized flow rate across the aperture, based on an experimental effort. This model is valid only in the zero-thickness limit, and it's applicability to more complex apertures is not known.
- **Impingement Flow**: Finally, the egress of the external environment is assumed to be arising from diffusion alone. The model does not take into account additional flux due impingement flow in a cleanroom or a spacecraft fairing environment.

In this paper we report on a combined experimental and numerical effort to characterize purge and infiltration in more detail. Although we concentrated only on water vapor, the findings should be applicable to molecular contamination in general. The goals of this effort concentrated on attempting to answer the above bullet points, although the final one, impingement flow, is left for future work. The experimental setup consisted of a long cylindrical pipe, capped at both ends, and containing optional internal baffle and secondary volume. The test volume was instrumented with multiple humidity and pressure sensors. Besides collecting data during purge, we also obtained data on water infiltration back into the cavity. The experimental setup is described in more detail in the following section. Following is a comparison of the experimental effort with the analytical model. The paper then continues with description of the numerical model. The ultimate objective of this effort is to develop a numerical tool capable of predicting contaminant concentration under various purge flow and geometry conditions. As will be apparent from the preliminary results, additional work still remains in achieving this goal. The paper is concluded with a summary of findings and future work.

2. EXPERIMENTAL SETUP

2.1 Test Enclosure

The test enclosure was constructed using a 2.5 ft long section of a size 10 schedule 40 cylindrical PVC pipe*. The geometry can be seen in Figure 1(a), and is further outlined in the drawing in Figure 1(b). The cylindrical

*Dimensions in this section are listed in imperial and SI units. The dimensions in imperial units correspond to measurements made in the laboratory using available tools. All dimensions were converted to SI for subsequent computations.

configuration was selected to allow for model comparison, since we anticipated development of an azimuthally-symmetric code. Size 10 PVC end caps were fitted to both ends to seal the volume, and 3/8" diameter holes were drilled in their centers. The depth of these holes was measured as 1.45 cm, which was slightly more than the typical thickness of the size 10 end cap. Due to the low inlet flow and hence low internal pressure, a friction fit between the end caps and the pipe was deemed sufficient to seal the volume. As can be seen from Figure 1(b), the length of the overlapping area was approximately 9 cm. A 1/4" AN bulkhead fitting was installed in the inlet cap to interface with the GN2 source. An additional 3/8" diameter hole was drilled in the cylinder at the midpoint to allow the pass-through of sensor wiring. This opening was sealed with multiple layers of Kapton tape. The volume of the test cavity was computed to be 0.0477 m^3.

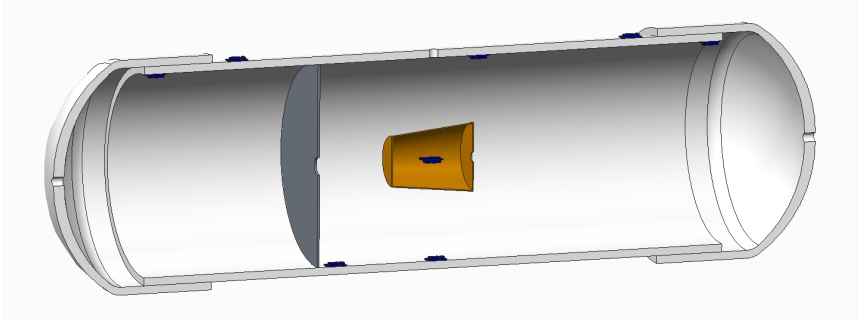

(a) Internal Geometry

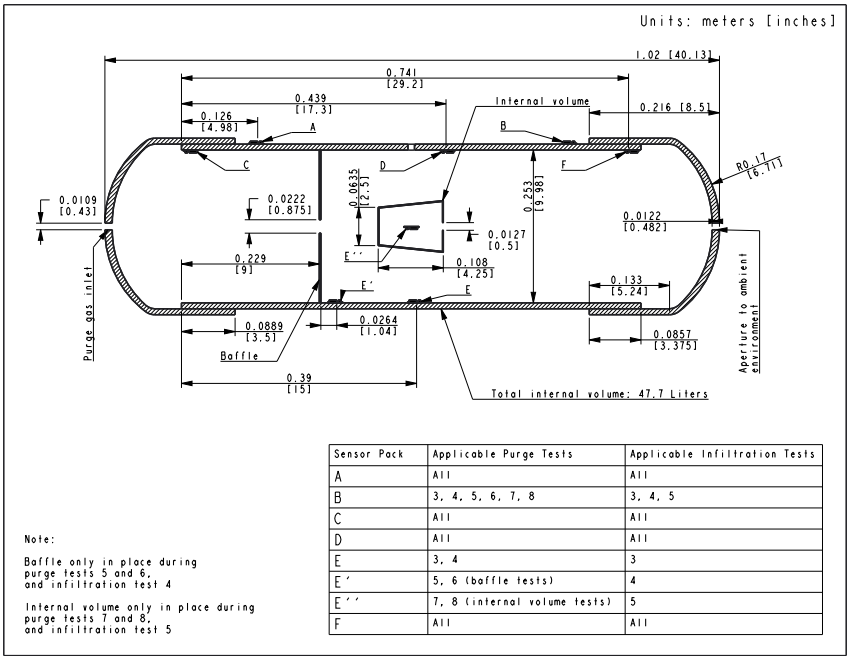

Sensor Pack	Applicable Purge Tests	Applicable Infiltration Tests
A	All	All
B	3, 4, 5, 6, 7, 8	3, 4, 5
C	All	All
D	All	All
E	3, 4	3
E′	5, 6 (baffle tests)	4
E′′	7, 8 (internal volume tests)	5
F	All	All

(b) Test setup dimensions and sensor locations

Figure 1. Figure (a) shows a CAD drawing of the test volume. Note that the combined baffle and internal volume configuration was not studied experimentally. Figure (b) shows the test dimensions and sensor locations.

The testing was performed at NASA Goddard Space Flight Center propulsion laboratory. The typical test setup is shown in Figure 2(a). Figure 2(b) shows the inside of the test cylinder for the case containing the internal baffle. An ultra high purity grade C gaseous nitrogen bottle source was used for most of the tests, except for the subset utilizing internal baffle or the cup. Grade C GN2 contains at most 5.7 ppmv (parts per million by volume) of water molecules.[4] These runs were conducted using a GN2 from a dewar boil-off, due to a temporary lack of an available gas bottle. An adjustable pressure regulator was used to dial the upstream pressure to 30

psig, and an adjustable 0.1-4 scfh float-type rotameter was used to establish the inlet flow rate. 1/4" PTFE and stainless steel flex hoses and 1/4" AN fittings were used as necessary to plumb the volume to gas source.

(a) Laboratory Setup (b) Internal View with Baffle Installed

Figure 2. (a) Photograph of a typical test setup in the NASA/GSFC propulsion laboratory. (b) View of onside of the test cylinder with the baffle installed, also showing the sensor packs.

The initial set of testing was performed with no obstruction in the test volume. This setup provided the simplest geometry, and also the closest correlation to the original Scialdone experiment. This configuration was tested at 2 scfh, 4 scfh, and 1 scfh. These flow rates approximately correspond to 1 L/min, 2 L/min, and 0.5 L/min, respectively. Subsequently, the impact of internal geometry was tested. First, an internal baffle with a small central opening was included, effectively separating the cylinder into two interconnected volumes. The baffle was constructed from an ESD bagging material, which was taped to the cylinder wall. The volume was also tested with the inclusion of a secondary internal volume with a single vent facing away from the purge inlet. The secondary volume was constructed by wrapping a coffee cup in foil, and suspending it from a sensor harness. These secondary volume tests added some complexity found in an actual instrument, while being sufficiently simple to allow correlation with the numerical analysis. All obstructed-flow testing was performed at a flow rate of 2 scfh. The tests are summarized in Table 1. At the conclusion of each test, the purge was discontinued, and the ambient environment was allowed to infiltrate back into the cavity.

Table 1. List of purge runs and configurations

Test No.	Configuration	Start Date	End Date	Flow Rate	Notes:
1	Unobstructed Volume	6/11/14	6/12/14	2 scfh	No temperature compensation
2	Unobstructed Volume	6/13/14	6/16/14	2 scfh	No temperature compensation
3	Unobstructed Volume	7/1/14	7/1/14	4 scfh	
4	Unobstructed Volume	7/7/14	7/9/14	1 scfh	
5	Internal Baffle	7/9/14	7/9/14	2 scfh	Flowmeter malfunction
6	Internal Baffle	7/10/14	7/11/14	2 scfh	
7	Secondary Volume	7/17/14	7/18/14	2 scfh	Loss of purge gas pressure
8	Secondary Volume	7/18/14	7/21/14	2 scfh	

2.2 Sensors

Sensor selection was an important part of the experimental effort. We were interested in obtaining the contaminant concentration and pressure at multiple locations, while at the same time minimizing the impact to the internal environment. As such, the sensors had to be both small in size, and also capable of measuring properties of interest across the expected range of values at a fast response rate. Ease of integration with a data acquisition system was also considered. The resulting selection consisted of analog relative humidity (RH),

absolute pressure, and temperature sensors. The analog output allowed rapid prototyping and the ability to quickly and easily diagnose both hardware and software issues during the development of the test setup. The individual sensors are described in more detail below.

The Honeywell HIH-5030 surface mount (SMT) sensor[5] was used to obtain the humidity data. This capacitive relative humidity sensor is only approximately 1 cm long, and is capable of measuring from 0 to 100% RH. Although absolute measures would be required for eventual correlation with numerical results, the limited availability, high cost, and comparatively large size of absolute humidity sensors precluded this option. Absolute humidity values must then be calculated from the relative humidity based on measured conditions (temperature and pressure) in the test volume. For the purposes of this experiment, this method would be sufficient to reliably measure the moisture levels in a volume under purge. Manufacturer provided operating specifications can be found in table 2. The HIH-5030 has an analog output which is ratiometric to relative humidity, $V_{out} = V_{supply} * (0.00636) * (RH) + 0.1515$. The supply voltage ($V_{supply}$) was 5 Vdc. Solving for RH, yields $RH = (V_{out}/V_{supply} - 0.1515)/0.00636$. The computed humidities were in a good agreement against a calibrated GE Parametrics PM880 hygrometer with a M2LR-00-010-0 probe.

Table 2. HIH-5030 Specifications

Parameter	Minimum	Maximum	Unit
Accuracy	-3	+3	% RH
Voltage Supply	2.7	5.5	Vdc
Operating Humidity	0	100	% RH

Absolute pressure was measured using the Freescale Semiconductor MPXHZ6130A sensor.[6] The sensor is a piezoresistive transducer with an analog output ratiometric to absolute pressure. Manufacturer specifications can be found in Table 3. Again, a transfer function was used to convert the sensor output voltage to pressure (in kPa), $P_{kPa} = (V_{out}/V_{supply} + 0.07739)/0.007826$.

Table 3. MPXHZ6130A Specifications

Parameter	Minimum	Maximum	Unit
Accuracy	-1.5	+1.5	kPa
Voltage Supply	4.75	5.25	Vdc
Operating Pressure	15	130	kPa

Temperature was obtained from Analog TMP36 sensor.[7] Local gas temperature was needed to convert relative humidity to absolute values. Since the experiment was conducted in a laboratory with limited control over the external air-conditioned environment, the temperature was seen to vary with a noticeable diurnal periodicity. Manufacturer specifications for this sensor can be found in Table 4. The measured temperature in (C) was given by $T = (V_{out} - 0.5) * 100$, where V_{out} is the sensor output voltage.

Table 4. TMP36 Specifications

Parameter	Minimum	Maximum	Unit
Accuracy	-1.5	+1.5	°C
Voltage Supply	2.7	5.5	Vdc
Operating Temperature	-40	125	°C

2.3 Data Acquisition

National Instruments LabVIEW is often the defacto data acquisition system for collecting experimental data. However, due to the limited license availability of a LabVIEW system, an alternative was required. Initial sensor selection, testing, and calibration was performed using an Arduino micro-controller board. After success in prototyping, this platform was selected to perform the actual data collection for testing. Although this approach required development of the micro-controller code, the Arduino approach resulted in an increased flexibility at a

fraction of the cost of a LabVIEW system. The small size of the micro-controller board allowed the experiment to be run in multiple locations, and be moved without much effort.

In order to easily interface the sensors with the Arduino, some hardware was necessary. The selection of surface mount (SMT) sensors required the use of SMT to DIP boards to allow connection to the Arduino (which uses standard 0.1" hole spacing). The humidity and pressure sensors were soldered to SOIC-14 SMT to DIP breakout boards, and male DIP headers were attached to the SOIC-14 boards. Wiring harnesses were made to provide power to the sensor packs, and to carry the sensor output voltages. Six sensor packs (including pressure and humidity sensors) and six wiring harnesses were assembled. A prototyping board with standard 0.1" hole spacing was used to wire the sensor packs to the Arduino in parallel via the wiring harnesses. Male headers allowed this board to be attached directly to the Arduino itself, and for power, ground, and all analog voltages to reach the appropriate ports. Figures 3(a) and 3(b) show the humidity and pressure sensors surface mounted to a SOIC-14 board and the wiring to the sensor pack, and the breakout board connecting sensor pack wiring to the Arduino for processing, respectively. The temperature sensors were not included in the sensor packs. Instead, one temperature sensor was suspended from a separate wire in the middle of the test volume. Another sensor was connected by a short (about 3cm) harness to the Arduino board.

Purge flow and moisture infiltration testing was conducted using multiple sensor configurations. Initially, three sensor packs were used to measure internal conditions at a location near the purge inlet, in the middle, and at a location near the aperture. The sensors were installed near the enclosure wall, by taping the harness to the wall using Kapton tape. One sensor pack was used outside. After two purge runs at 2 scfh and subsequent humidity infiltration tests additional pressure and humidity sensors were added to the test volume. Locations for all setups can be found in Figure 1(b). The initial purge runs did not contain an internal temperature sensor, and used data from the external sensor for calculation of the absolute humidity.

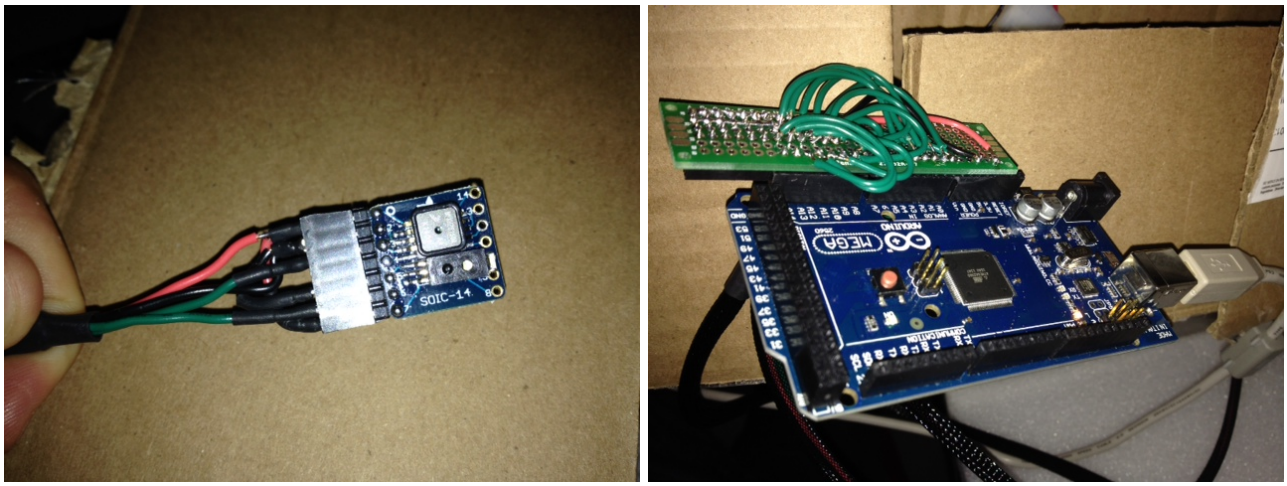

(a) Sensor pack with wiring harness (b) Arduino Mega with breakout board

Figure 3. (a) Sensor pack containing one pressure and one humidity sensor, and (b) Arduino board used for data acquisition

2.4 Software

Figure 4 shows an overview of the data acquisition system and the processing performed by the Arduino. Analog values were constantly sampled by the Arduino micro-controller's on-board analog to digital converter (ADC), and stored in a rolling buffer. These values were passed through a inter-quartile-range (IQR) filter in order to reject outliers. The remaining data was averaged and output over the serial communications port at a specified rate (every 10 seconds for this experiment).

A simple Java program was written in order to read the values transmitted by the Arduino over the serial port. This code operates separately from the Arduino, which reads and processes data whenever powered. When run, the Java program receives incoming serial data as a string of values, parses this string to find values to

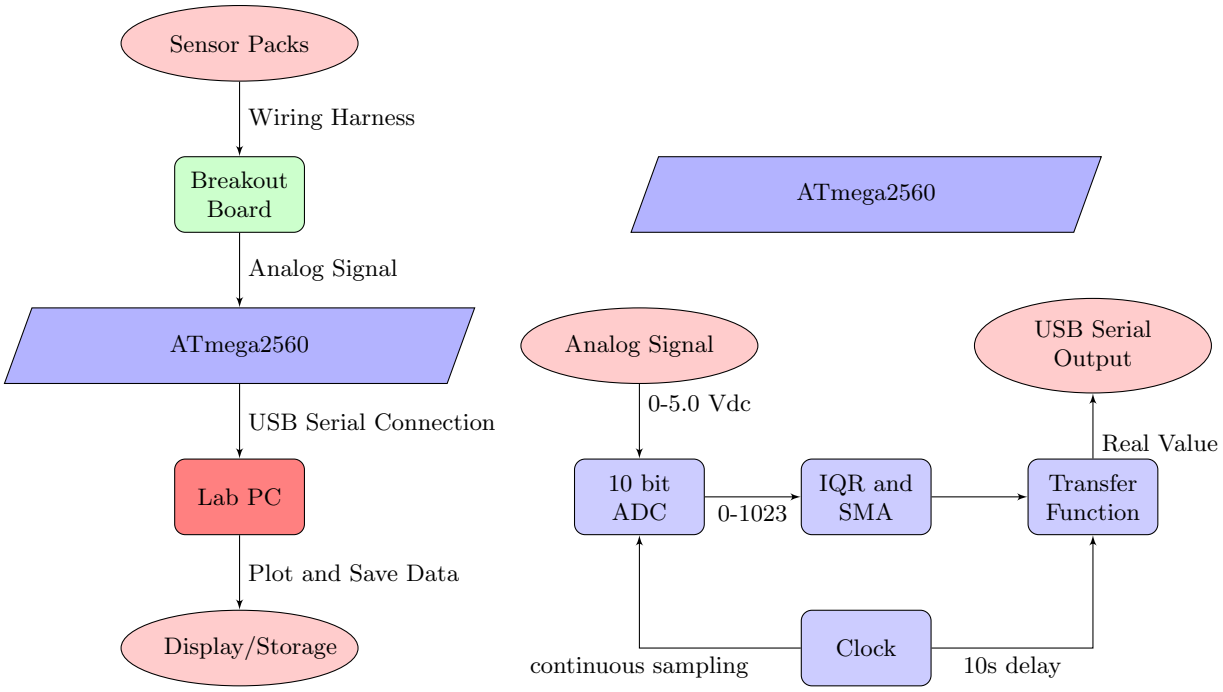

(a) Data Acquisition System (b) Signal Processing

Figure 4. Schematic of the data acquisition system

be plotted, and writes the string to a plain-text .csv file. This file can then be read by Excel or MATLAB for further analysis.

2.5 Data Reduction

Correlation of sensor data with the analytical model requires computing the absolute humidity, which is a function of saturation vapor pressure of the system, $p_{w,s}$. Multiple models exist for this value. In this work, we utilized a model from NOAA,[8]

$$p_{w,s}(\text{kPa}) = 0.611 * 10^{(7.5*T)/(237.3+T)} \tag{5}$$

where T is in Celsius. With the saturation vapor pressure known, the relative humidity, $RH = (p_w/p_{w,s}) \cdot 100\%$ can be converted to absolute humidity in parts per million by volume (ppmv) as

$$ppmv_w = \frac{(RH/100\%)p_{w,s}}{p_{tot}} \cdot 10^6 \tag{6}$$

where p_{tot} is the total pressure. Values in ppmv can also be converted to number density utilizing the ideal gas law $p = nkT$,

$$n_w = \frac{ppmv_w}{10^6}\frac{(p_{tot})}{kT} \tag{7}$$

To illustrate the conversion, consider the data shown in Figure 5(a). The blue and green traces show the RH values obtained from an external and an internal sensor. The red trace is the temperature. Using the above relationship, the two RH curves are converted to absolute values in Figure 5(b). Note the smoothening of the internal humidity curve upon conversion to absolute values. This figure also illustrates the typical variation in the external humidity during testing.

3. EXPERIMENTAL DATA

Figure 6(a) shows the typical sensor response during an empty cavity run. This particular set of data came from Test No. 3 with a 4 scfh purge rate, but it is characteristic of the runs at the other two flow rates as well. The

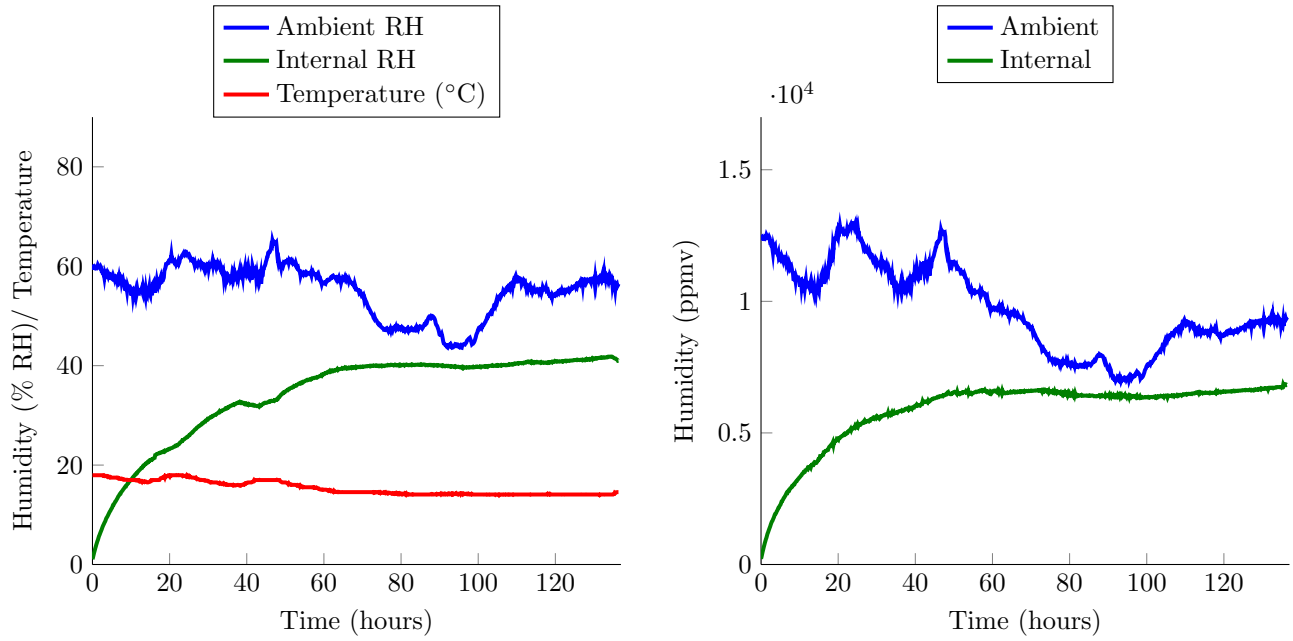

(a) Raw Data (b) Converted Data

Figure 5. Computation of absolute humidity. Figure (a) shows relative humidity and temperature obtained from the internal sensors. These are used to compute the absolute humidity in (b).

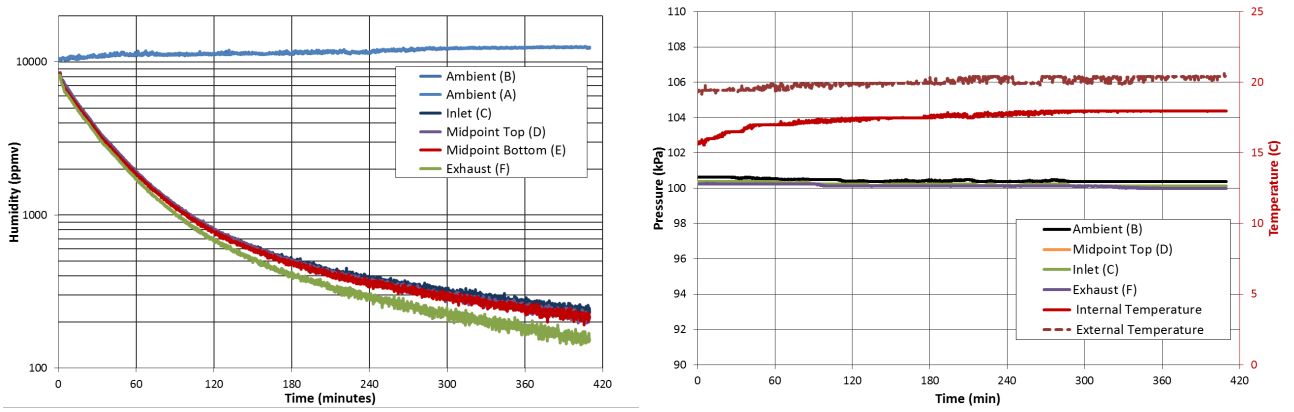

(a) sensor data (b) pressure and temperature

Figure 6. Experiment results for 4 scfh (∼2 L/min) flow rate purge. Note the tendency for lower humidity in the flow direction in (a), and no impact of purge on pressure and temperature in (b).

figure plots the internal and external humidity, in parts per million. The humidity data is shown on a log scale. As can be seen from this figure, very little difference was observed between the 3 internal sensor locations (near the end cap containing the inlet, at the midpoint, and near the end cap containing the open aperture). The difference becomes apparent only once the concentration drops below 500 ppvm, corresponding roughly to 2.5% RH. It is interesting to note that the water content decreases with decreasing distance to the aperture. This was unexpected, since we anticipated the highest concentration near the aperture due to water infiltration from the ambient environment. Likely, the finite speed of the purge gas moving through the aperture resulted in an advective term preventing additional diffusion from the external environment.

Figure 6(b) shows the internal and external temperature and pressure for this same run. By looking at this plot alone, it is not possible to determine when the purge flow was initiated. As such, we can note that the

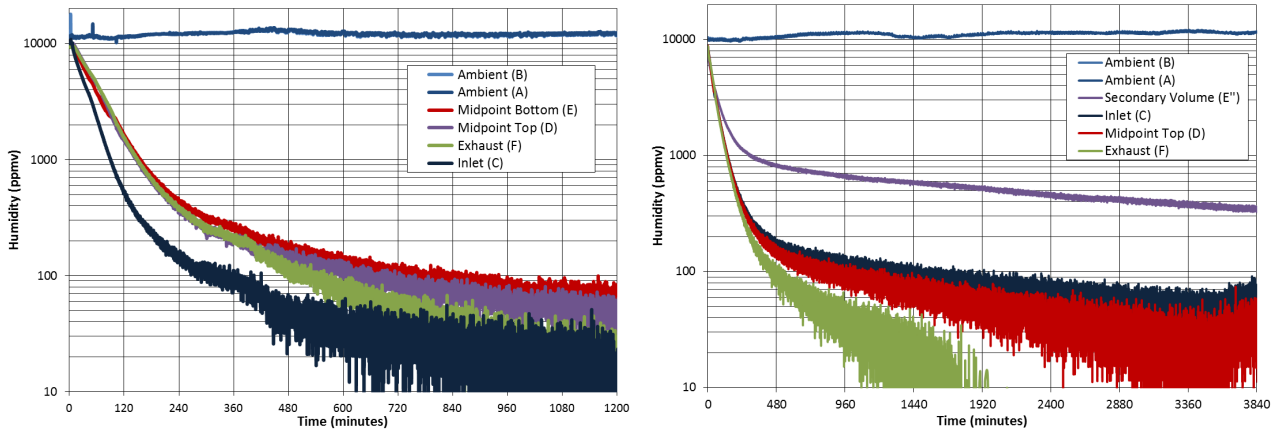

(a) baffle (b) secondary volume

Figure 7. Internal humidity data for the configurations including internal obstructions: (a) baffle (run 6), (b) secondary volume (run 8).

purge gas does not have a significant impact on the internal temperature and pressure. The pressure drop that forms in response to the moving fluid is too small to detect with these sensors. The slight difference between the internal and external temperature readouts was attributed to a faulty sensor, and following this run, the second sensor was replaced with a new unit.

The variation in internal humidity becomes more pronounced once additional objects are included in the test cavity. These results can be seen in Figure 7. The first plot shows the results for the test with the baffle. The second plot shows corresponding results for the case with the secondary volume, constructed from a coffee cup wrapped in foil. Impact of the secondary volume can be seen in both sets of results. The baffle can be seen to reduce the water vapor concentration in the zone containing the purge inlet. Water concentration in this zone is approximately 3 times smaller than in the downstream zone. In the case of the secondary volume, the water concentration inside the cup is approximately 7 times greater than outside. This can be attributed to the cup aperture facing away from the purge inlet. As such, it is difficult for the purge gas to enter the secondary volume and carry away the water vapor. The removal of water vapor from within the secondary volume is then governed by diffusion arising from the the concentration gradient across the aperture. This behavior can be seen in the simulation results presented in section 4.

3.1 Purge Model Correlation

The Scialdone model was derived assuming an empty volume, and as such, only the results from the empty cavity runs were compared against the model. Since very little variation was seen in the sensors, it made sense to average the internal sensors into a single corresponding trace. These results are plotted in Figure 8. The solid red line shows the results from the 4 scfh case, which were presented previously in Figure 6(a). The black and blue traces correspond to 2 scfh and 1 scfh, correspondingly.

The Scialdone model is governed by four sets of parameters: normalized purge flow rate Q/V, normalized infiltration rate C/V, the ambient partial pressure P_0, and the initial partial pressure P_i. Since this model governs the rate of change of some quantity, the initial and ambient concentrations in ppmv can be substituted in lieu of the partial pressures. The Q/V parameter can also be easily computed from the known values of the flow rate Q and the enclosure empty volume V. The second parameter, C/V is not so easy to determine. As noted by O'Hanlon,[9] in the continuum regime, volumetric flow rate through a short round tube does not have a simple analytical form. Scialdone performed a set of experiments to characterize the C value. Results from his study are shown in Figure 3 in Reference 2. These results are given as a function of V/A, the volume of the test cavity divided by the aperture area. As such, it safe to assume that the given form is valid only in the limit of thin orifices. The plot lists the relationship for the time constant $\tau_v \equiv V/C$ as $\tau_v = 0.42 \cdot 24 \cdot (V/A)$, where V/C is in hours and V/A in meters. This equation is likely a typo, as the correct form should contain the exponent

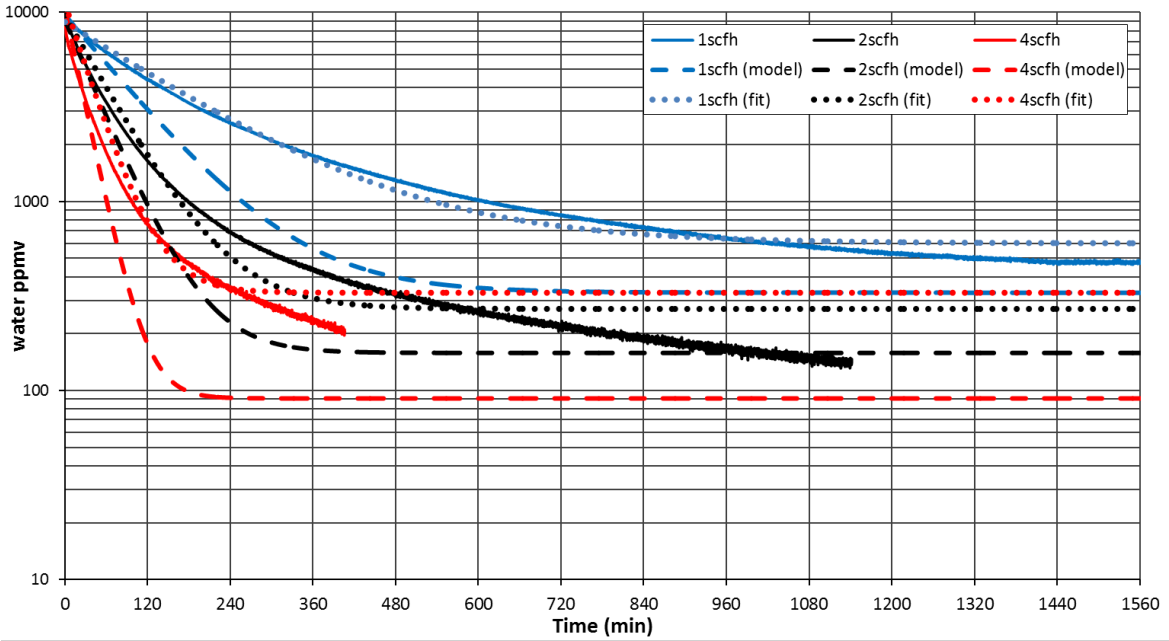

Figure 8. Comparison against the analytical model. The dashed lines show the predicted water vapor decay using known Q/V values in the Scialdone model.

Table 5. Fit parameters to experimental purge data for $p = a\exp(-bt) + c$, t in hours

flow rate	a	b	c
2 scfh	9412.3	0.9182	270.27
4 scfh	10870.0	1.58895	329.15
1 scfh	8308.5	0.34059	600.38

of 0.25 to match the data on the log-log plot, $\tau_v = 0.42 \cdot 24 \cdot (V/A)^{0.25}$. Scialdone in fact alludes to this 0.25 exponent in his earlier paper.[1] Using the correct form of the equation, the ratio C/V can be computed as 0.0208 hrs. Multiplying by volume, we obtain $C = 9.95 \times 10^{-4}$ m^{-3}/hr.

Using these values, the analytical model can be plotted. It is shown by the dashed line in Figure 8. As can be seen, the agreement is only somewhat satisfactory, with a common trend existing in all three sets of curves. The analytical model predicts a must faster initial depletion of the contaminant than seen experimentally. For instance, at $t = 120$ min, the model predicted water vapor concentrations 1.5, 1.8, and 4.34 times smaller than seen experimentally for 1, 2, and 4 scfh, respectively. The steady state value also differs between the experiment and the prediction. The sensor data indicate concentrations continuing to decay well past the time when steady state was predicted by the model. Unfortunately, the 4 scfh run did not last long enough to obtain the steady state value. However, by looking at the trend, it appears that both the 4 scfh and the 2 scfh cases resulted in steady state water concentrations below the predictions, while the 1 scfh run resulted in a steady concentration higher than predicted.

In order to study the discrepancy further, we fitted the experimental data to an equation of form $p = a\exp(-bt) + c$. The fit coefficients are listed in Table 5 and the curves are plotted in Figure 8 with the dotted line. These fits also fail to predict the correct steady-state behavior, indicating that the response of the real system contains terms beyond the single exponential model. However, considering the fit parameter $b = (C + Q)/V$ allows us to obtain additional information about the test. Of main interest is comparing the expected purge flow rate to characteristic value obtained from the experiment. Using the previously determined value of C, we obtain the characteristic flow rates listed in Table 6. The computed errors are well within the expected range of experimental error. In all three cases, it appears that the supplied purge flow rate was less than indicated by the flow meter.

Table 6. Set and determined purge flow rates

Flow Rate	Q (m^3/hr)	Q fit (m^3/hr)	Error (%)
2 scfh	0.0567	0.0428	24.4
4 scfh	0.113	0.0748	34.0
1 scfh	0.0283	0.0153	46.1

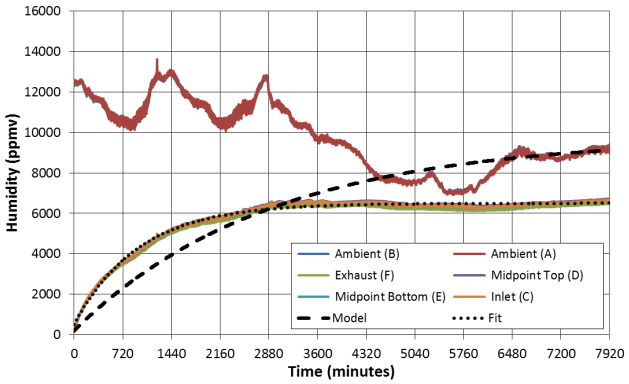

(a) empty volume

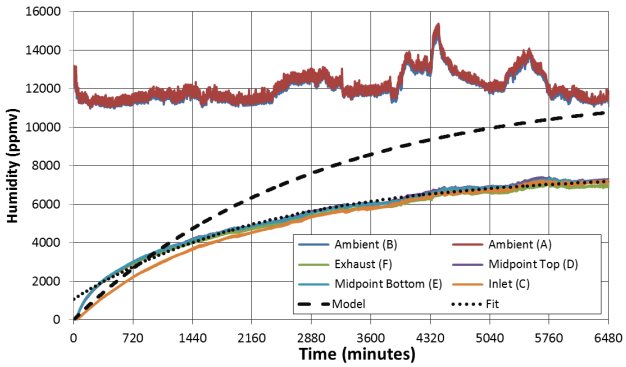

(b) baffle

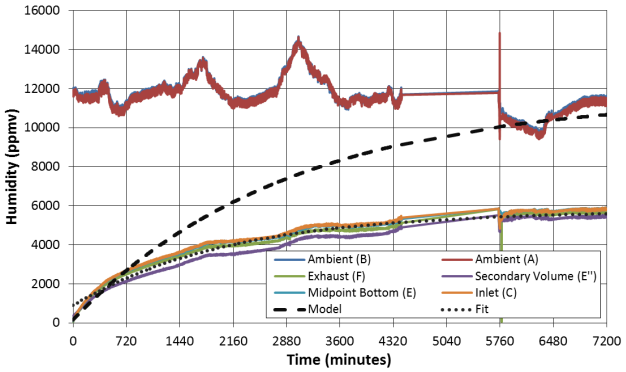

(c) secondary volume

Figure 9. Water vapor infiltration into the cavity once the purge was stopped. The dashed line indicates the predicted response from the analytical model.

;

3.2 Water Infiltration

At the conclusion of each purge run, the flow was discontinued, and data collection was continued to obtain data on water infiltration. These results are presented in Figure 9. This figure plots the water infiltration results for three cases: empty cavity (corresponding to the end of Test No. 3), run with the baffle, and test with the secondary volume. Data from all internal and external sensors is plotted. As before, the two ambient sensors resulted in identical values. Similar trends can also be seen in the internal data, with very little variation seen in the empty cavity run. Inclusion of the internal geometry shows an impact on the sensor data. As expected, the area behind the baffle remains drier longer than the volume closer to the inlet aperture. Similarly, we can see lower internal humidity inside the secondary volume in Figure 9(c).

The dashed line in all three plots is the predicted infiltration rate from Equation 3. A noticeable difference can be seen in both the infiltration rate, and the steady-state behavior. The model predicts an exponential growth until the internal concentration equilibrates with the ambient environment. This however was not seen experimentally. Instead, in all infiltration cases, the internal humidity leveled off at values ranging from 50 to 73% of the ambient. From Equation 2, it can be seen that independent of the value of C, $P \to P_0$ as $t \to \infty$ if $Q = 0$. This discrepancy is believed to arise to a finite concentration drop across the finite thickness aperture,

Table 7. Fit parameters to experimental infiltration data for $p = a\exp(-bt) + c$, t in hours

case	a	b	c
empty	-5983.3	-0.0628	6501.3
baffle	-6558.0	-0.0248	7626.6
cup	-4857.8	-0.02839	5749.7

which is not taken into account in the model, which was derived assuming a zero-thickness orifice. Although not shown in the plot here, at the conclusion of each infiltration case, we removed the end cap and saw the internal sensors immediately equilibrate with the ambient reading.

We can also use these infiltration results to obtain a new estimate for C. The experimental data was fitted to an exponential of form $p = a\exp(-bt) + c$ using the online equation fitter at `zunzun.com`. The equation fits are shown with a dotted line and the coefficients are listed in Table 7. Of note is the parameter $b =\equiv C/V$. The average of these three cases is 0.03869, which is 85% larger than the 0.02086 value computed from $V/C = 0.42 \cdot 24 \cdot (V/A)^{0.25}$. The actual conductance across the aperture was higher in the experiment than expected. On the other hand, the infiltration rate decreased as the internal concentration started approaching the ambient environment. This finding indicates that the conductance term C is not a constant, but is instead a function of the concentration gradient, $C = C(\nabla c)$, as well as geometry.

3.3 Sensitivity Studies

Finally, returning to Figure 8 and Equation 3, it is possible to study the sensitivity of different parameters on the goodness of the fit. This study is presented in Figure 10 for the 2 scfh data set. The thick black line shows the trace noted before, using the expected values for Q and C. The impact of error in the flow rate is plotted with the dashed line. The red trace shows the deviation from the baseline if the flow rate is increased by 30%. The blue line is the counterpart to lower than expected flow rate. As can be seen, neither curve results in a good agreement, but improvement is seen for $Q < Q_{input}$. This was noted previously, and could be an indication of flow meter calibration issues. The impact of the conductance parameter C is shown with the black dotted line. This trace shows prediction using the calculated Q, but using C obtained from the infiltration experiment discussed in the previous section. The impact of the purge flow impurities is shown with the thin blue line. Here we assumed that the purge flow contains 5× the amount of water allowed for a grade C gas.

Alone, neither case results in a significant improvement. Combining the reduced flow rate and the experimentally determined C does however result in a notable improvement, at least for the initial decay. This plot is shown in green. The steady-state response is however incorrect, as was the case with the other cases. This may again be an indicator of the pressure and time dependent variation in the C term. It may also be an indicator of surface processes such as desorption and adsorption taking place. The yellow trace shows the model prediction for comparable to the green trace, but with the constant $(CP_0 + QP_u)/(C + Q)$ term multiplied by $\exp(-(C + Q)/V(0.06t)$. This double exponential form results in a much improved agreement, but the physical meaning of this fit still remains to be investigated. It should be pointed out that this double exponential form will result in the internal pressure approaching zero which is a non-physical finding if any sources of the contaminant exist in the enclosure

4. NUMERICAL MODEL

In addition to the experimental effort, we also performed an initial study of the purge and infiltration behavior using numerical analysis. Transport of a contaminant in a moving medium is governed by the advection-diffusion (AD) equation. This equation describes the temporal evolution of concentration of some species due to three contributions: diffusive flux, advective flux, and the production rate. Diffusive flux is governed by Fick's law, $\vec{j}_{diff} = -D\nabla c$. This law describes the transport due to a concentration gradient ∇c, arising from the natural tendency of systems to drive towards equilibrium. Advective flux governs transport due to velocity of the medium in which the contaminant is dispersing. This term is given by $\vec{j}_{adv} = \vec{v}n$. Inserting the two flux terms into the mass conservation equation, $\partial c/\partial t + \nabla \cdot \vec{j} = R$, yields the advection-diffusion equation,

$$\frac{\partial c}{\partial t} + \nabla \cdot (-D\nabla c + \vec{u}c) = R \tag{8}$$

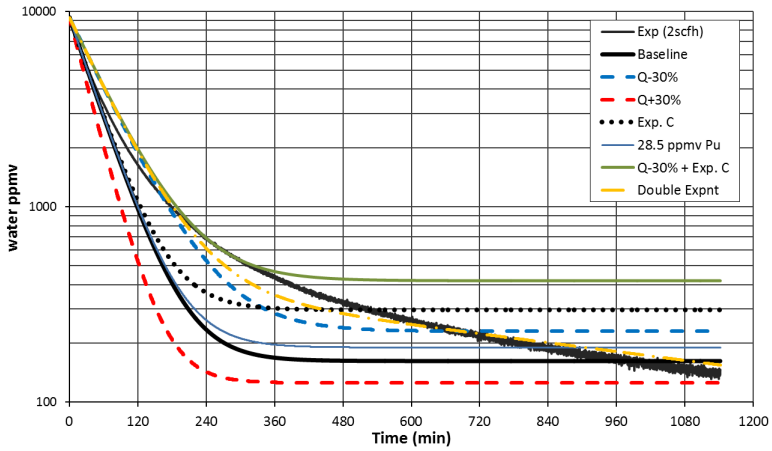

Figure 10. Impact of various parameters on the correlation of the Scialdone model with experimental data. The double exponential curve plots a hypothetical model in which the constant $(CP_0 + QP_u)/(C + Q)$ terms decays as an exponential of time.

where c is concentration of the contaminant. In this work, the concentration was set to the number density n, given in units of number of molecules per m^3. The source term R governs a volumetric mass creation (for instance due to a chemical reaction), and was set to zero in the simulation. Instead, the ambient environment was introduced through the boundary conditions. The binary diffusion coefficient D was set to 0.256×10^4 m^2/s per Ref. 10.

Computing the advective flux requires information on the velocity of the medium. In the case of the purge flow, this is the nitrogen gas velocity, and it can be calculated from the Navier-Stokes (NS) equations. Since the flow speed ($u = Q/A$) was highly subsonic, the incompressible form of the NS equations can be utilized. It is given by

$$\frac{\partial \vec{u}}{\partial t} + \vec{u}\nabla \cdot \vec{u} = -\frac{1}{\rho}\nabla p + \frac{\mu}{\rho}\left(\nabla^2 \vec{u}\right) \tag{9}$$

From the saturation vapor pressure equation 5, it can be seen that the water forms only about 1% of the total atmospheric pressure. As such, it is safe to assume that the purge flow will not be affected by the concentration of the water vapor. This then allows us to decouple Equation 9 from Equation 8. The solution can be obtained by first using the Navier-Stokes equation to march the velocity field forward, then using the newly computed velocity to update the water concentration, and finally repeating the process until the specified amount of real time is simulated. In order to speed up the calculation, the simulation was performed on a two-dimensional azimuthally-symmetric (RZ) domain. The following paragraphs describe details of the two solvers, and also present the preliminary simulation results. The code was developed in Java. Subset of the cases was executed on the Amazon Web Services Elastic Compute Cloud (AWS EC2), with the rest executed on a desktop workstation. For the case of infiltration (with no purge flowing), the code was able to compute a weeks worth of results in about a day.

4.1 Advection-Diffusion Solver

Both the AD and NS equations were solved using the Finite Volume Method (FVM) with a staggered grid. This approach is particularly suitable to this problem since it easily allows setting of zero-flux condition on solid walls. In the FVM approach, the computational domain is divided into cells (control volumes). Quantities of interest are assumed to be known at cell centers. Fluxes and velocities are known along cell edges, resulting in a staggered grid. Discretization equations are computed by rewriting the governing equation using the divergence theorem to obtain surface integrals. To illustrate this method, let's consider the AD equation 8. We take volume

and time integral of both sides,

$$\int_V \int_{t_0}^{t_0+\Delta t} \frac{\partial c}{\partial t} dt dV = \int_{t_0}^{t_0+\Delta t} \int_V \nabla \cdot (D\nabla c - c\vec{v}) + R dV dt$$
$$\left(c^{t_0+\Delta t} - c^{t_0}\right) \Delta V = \int_{t_0}^{t_0+\Delta t} \left[\int_S (D\nabla c - c\vec{v}) \cdot \hat{n} dA + \int_V R dV \right] dt$$

where the right hand side was rewritten using the divergence theorem. In addition, we rewrite the surface integral as a summation over the four sides of our 2D control "volume" (the computational cell). Also, we label the current time t_0 with the subscript k and the next time step with the subscript $k+1$. The difficulty in evaluating the above equation is deciding at what time should the RHS be evaluated. The approach used in this code was to use the Crank-Nicolson (CN) method. This is a numerically stable method in which the RHS is evaluated at time half way between the old and new time step.[11] We obtain

$$\left(c^{k+1} - c^k\right) \Delta V = 0.5 \left[\sum_{i=1}^{4} \left(D\nabla c^k - c^k \vec{v}^k\right) \cdot \hat{n} \Delta A + \sum_{i=1}^{4} \left(D\nabla c^{k+1} - c^{k+1}\vec{v}^{k+1}\right) \cdot \hat{n} \Delta A + \left(R^k + R^{k+1}\right) \Delta V \right] \Delta t$$

The CN formulation leads to an implicit method, since values at $k+1$ are required to advance to step $k+1$. The above system can be written in a matrix form,

$$\mathbf{A} c^{k+1} = \mathbf{B} c^k + 0.5 \left(R^{k+1} + R^k\right) \tag{10}$$

where R is a source term that is assumed to be known at time $k+1$. Moving all $k+1$ terms to the left side, we have

$$c^{k+1} - \frac{\Delta t}{2\Delta V} \left[\sum_{i=1}^{4} \left(D\nabla c^{k+1} - c^{k+1}\vec{v}^{k+1}\right) \cdot \hat{n} \Delta A \right] = c^k + \frac{\Delta t}{2\Delta V} \left[\sum_{i=1}^{4} \left(D\nabla c^k - c^k \vec{v}^k\right) \cdot \hat{n} \Delta A \right] + \frac{\Delta t}{2} \left(R^k + R^{k+1}\right)$$

or

$$\left(\mathbf{I} - \mathbf{M}^{k+1}\right) c^{k+1} = \left(\mathbf{I} + \mathbf{M}^k\right) c^k + 0.5(R^{k+1} + R^k) \tag{11}$$

The coefficients are computed by summing over the four faces of a two-dimensional cell. For a rectilinear cell, they are the East, North, West, and South faces. We use the standard central difference for the divergence, and approximate concentration at the cell edges as the average of the two neighboring cells. The $(D\nabla c - \vec{v}c) \cdot \hat{n} \Delta A$ term then evaluates as follows

$$\begin{aligned}
\text{East:} &\quad \left(\tfrac{D}{\Delta z}(c_{i+1,j} - c_{i,j}) - \tfrac{1}{2}(c_{i+1,j} + c_{i,j}) u_{i+1,j}\right) r_j \Delta r \\
\text{North:} &\quad \left(\tfrac{D}{\Delta r}(c_{i,j+1} - c_{i,j}) - \tfrac{1}{2}(c_{i,j+1} + c_{i,j}) v_{i,j+1}\right) r_{j+0.5} \Delta z \\
\text{West:} &\quad -\left(\tfrac{D}{\Delta z}(c_{i,j} - c_{i-1,j}) - \tfrac{1}{2}(c_{i,j} + c_{i-1,j}) u_{i,j}\right) r_j \Delta r \\
\text{South:} &\quad -\left(\tfrac{D}{\Delta r}(c_{i,j} - c_{i,j-1}) - \tfrac{1}{2}(c_{i,j} + c_{i,j-1}) v_{i,j}\right) r_{j-0.5} \Delta z
\end{aligned}$$

The above terms are multiplied by $\Delta t/(2 r_j \Delta z \Delta r)$, and we can simplify the coefficient equations using $\alpha_z = D\Delta t/(2\Delta^2 z)$, $\beta_z = \Delta t/(4\Delta z)$, $\alpha_r^+ = D r_{j+0.5} \Delta t/(2 r_j \Delta^2 r)$, $\beta_r^+ = r_{j+0.5}\Delta t/(4\Delta r)$, $\alpha_r^- = D r_{j-0.5}\Delta t/(2 r_j \Delta^2 r)$, $\beta_r^- = r_{j-0.5}\Delta t/(4\Delta r)$, and $\gamma = \Delta t/2$. By collecting terms, we can write the contributions to the $\mathbf{B}$ matrix:

	Center	East	North	West	South
$c_{i,j}$	1	$-\alpha_z - \beta_z u_{i+1,j}$	$-\alpha_r - \beta_r^+ v_{i,j+1}$	$-\alpha_z + \beta_z u_{i,j}$	$-\alpha_r^- + \beta_r^- v_{i,j}$
$c_{i+1,j}$		$\alpha_z - \beta_z u_{i+1,j}$			
$c_{i,j+1}$			$\alpha_r - \beta_r^+ v_{i,j+1}$		
$c_{i-1,j}$				$\alpha_z + \beta_z u_{i,j}$	
$c_{i,j-1}$					$\alpha_r^- + \beta_r^- v_{i,j}$

and similarly for the **A** matrix (note, velocities here are at the $k+1$ time):

	Center	East	North	West	South
$c_{i,j}$	1	$\alpha_z + \beta_z u_{i+1,j}$	$\alpha_r + \beta_r^+ v_{i,j+1}$	$\alpha_z - \beta_z u_{i,j}$	$\alpha_r^- - \beta_r^- v_{i,j}$
$c_{i+1,j}$		$-\alpha_z + \beta_z u_{i+1,j}$			
$c_{i,j+1}$			$-\alpha_r + \beta_r^+ v_{i,j+1}$		
$c_{i-1,j}$				$-\alpha_z - \beta_z u_{i,j}$	
$c_{i,j-1}$					$-\alpha_r^- - \beta_r^- v_{i,j}$

4.2 Boundary Conditions and Geometry

There are two types of boundary conditions applicable to the advection-diffusion equation: specified concentration, and specified normal flux. The specified concentration simply prescribes the value of c along the Dirichlet boundary, $c = g(s) \in \Gamma_D$. The specified flux boundary is derived as $\left(\vec{j}_{adv} + \vec{j}_{diff}\right) \cdot \hat{n} \equiv (c\vec{v} - D\nabla c) \cdot \hat{n} = h(s) \in \Gamma_R$. Specifically for the zero flux boundary, we have $(c\vec{v} - D\nabla C) \cdot \hat{n} = 0$. Specifying this boundary condition in the finite volume method is easy - the terms are simply not included for the zero-flux faces.

The zero-flux boundary was applied along all solid walls. The geometry of the problem was set from information presented in the drawing in Figure 1(b) by "sugar cubing" the internal cells. The location of each cell's centroid was computed, and if the location was outside the fluid domain, the entire cell was marked as solid. Outside the tube, the computational domain contained a section representing the ambient environment. The outer z and r edges of this ambient zone were set to a time-varying Dirichlet condition, with concentration varying according to the experimentally-collected ambient humidity data, e.g. the blue curve in Figure 5(b). The zero flux boundary was also applied along the axis of symmetry, $(\vec{j} \cdot \hat{e}_r)_{r=0} = 0$.

4.3 Infiltration Results

Figure 11(a) shows a snapshot of the computed water vapor density for a hypothetical case containing both the baffle and the secondary volume. This figure is meant to illustrate the variation in the internal contaminant concentration once a complex internal geometry is considered. The baffle is seen to have a noticeable affect on reducing the infiltration rate to the region located behind the baffle. Variation can also be seen between the water vapor concentration inside the secondary volume, however, at the particular time of this snapshot, the internal concentration is becoming comparable to that of the surrounding cavity.

This figure also illustrates the small external region corresponding to the ambient environment. A closeup of this region is shown in Figure 11(b). This figure plots the cell-centered concentration values and also illustrates the "sugar-cubing" of the geometry. Of importance is the concentration gradient that develops across the aperture. This is an artifact of a finite-thickness aperture, and is believed to be the reason for the internal concentration not reaching the ambient humidity, even after a prolonged infiltration test.

In addition to being able to obtain the graphical representation of the two-dimensional variation in the contaminant concentration, the simulation code was also instrumented with virtual sensors that collected local pressure and humidity as a function of time. The location of these sensors was selected according to the experimental sensor placement. The comparison between the numerical and experimental data can be seen in Figure 4.3. This figure plots results for an empty cavity case, in which neither the baffle nor the cup were present. The black line is the ambient humidity which was used to set the ambient Dirichlet boundary condition. As can be seen, the numerical predictions are in line with the experiment, however, a noticeable discrepancy exists. The simulation seems to predict a similar asymptoting behavior, however the rate of infiltration increase differs from data. Specifically, the experiment resulted in a faster initial build up of the water vapor, followed by a rapid decay in rate. The simulation on the other hand resulted in a much more linear response. The spatial difference in sensor data was also greater for the numerical case. These discrepancies will be investigated as part of future work. One possible explanation is that the experimental case includes additional sources of water, such as surface desorption, that are not included in the experiment.

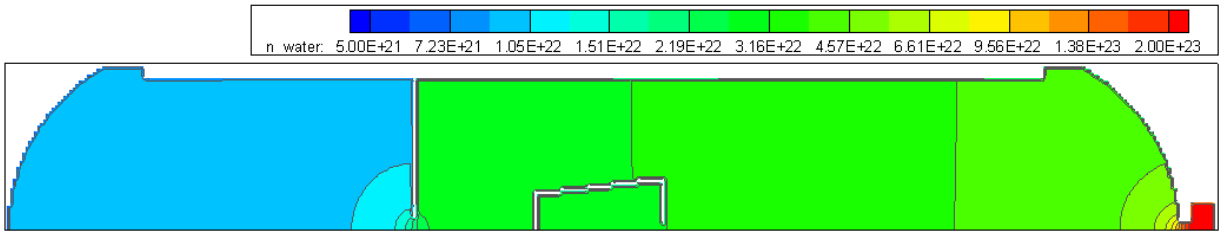

(a) water vapor density

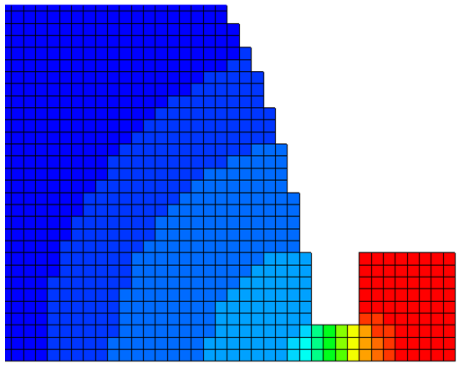

(b) aperture closeup

Figure 11. Numerical results for the infiltration case ($Q = 0$). Figure (a) shows water vapor density for a hypothetical configuration containing both the baffle and the secondary volume. Figure (b) shows a closeup of the aperture area.

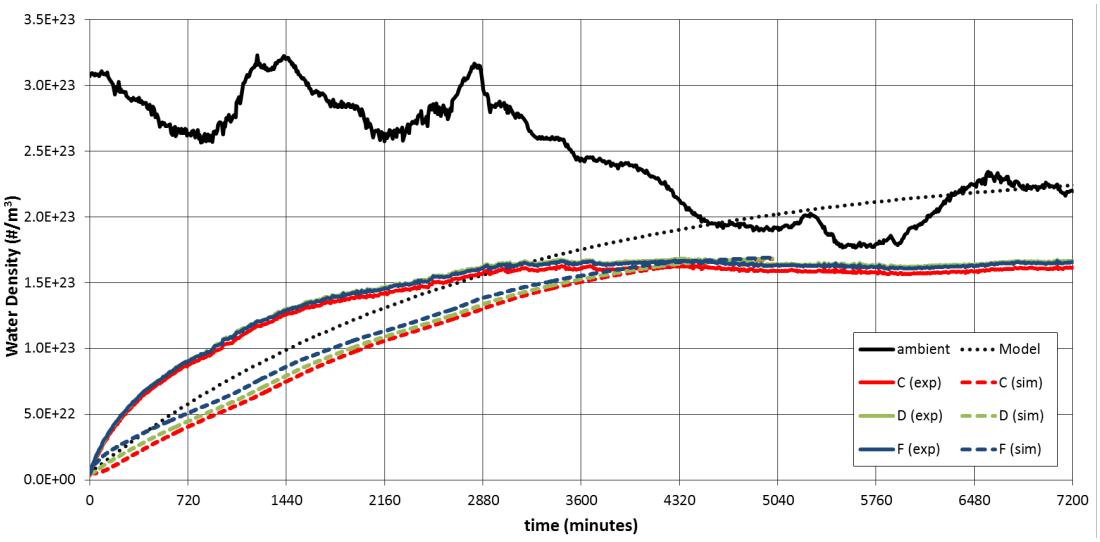

Figure 12. Comparison of empty volume infiltration simulation case with experimental data.

4.4 Navier-Stokes Solver

The incompressible Navier-Stokes equation 9 is solved using the projection method.[12] In this method, the velocity update is split into two parts: a part due to advection and viscous diffusion, and a part due to the pressure gradient. First, a temporary velocity is computed,

$$\frac{\vec{u}^t - \vec{u}^k}{\Delta t} = -\vec{u}^k \nabla \cdot \vec{u}^k + \nu \left(\nabla^2 \vec{u}^k\right) \tag{12}$$

Then, the pressure gradient is added to obtain the velocity at the next time step,

$$\frac{\vec{u}^{k+1} - \vec{u}^t}{\Delta t} = -\frac{1}{\rho} \nabla p \tag{13}$$

Since from mass conservation $\nabla \cdot \vec{u}^{k+1} = 0$, we can write

$$\frac{\Delta t}{\rho} \nabla^2 p = \nabla \cdot \vec{u}^t \tag{14}$$

This Poisson's equation is solved using the preconditioned conjugate gradient (PCG) solver, which is also used in the implicit AD code. The resulting pressure field is then used in Equation 13 to compute the new velocity field.

The NS solver also utilizes a staggered grid with pressure known at the cell center, and velocities known at the midpoint of the cell edges. The boundary conditions for the solver included zero velocity along walls (no-slip condition) and no flow across the axis of symmetry. A well-developed flow $\partial u/\partial r = 0$ was specified at the outflow boundary. The purge flow was specified by setting $u = u_{inlet}$ along cell edges corresponding to the purge inlet.

4.5 Preliminary Purge Flow Results

Unlike the AD code, the NS solver utilized an explicit time integration scheme, and as such required smaller time steps than allowed under the implicit scheme. Yet even with smaller time steps that satisfied the CFL condition, the combined AD+NS approach was found to result in regions with negative density. This finding is likely indicative in a remaining bug in the solver that will be investigated as part of future work. The results presented in this section were computed using a density limiter $n > 1e19m^{-3}$. Presence of such a limiter however results in an artificial mass increase, since contaminant concentration is numerically increased if it falls below the threshold value.

The preliminary purge flow simulation results are shown in Figure 13(a). This figure plots the water vapor concentration for the hypothetical case containing both the baffle and the cup, with the initial internal concentration equal to the ambient environment, and purge flow rate $Q = 1$L/min. Figure 13(b) shows the flow speed at the corresponding time. As expected, the flow speed is increased whenever the flow encounters an obstruction, such as the baffle opening or the exit aperture. We can also note from these plots the impact of advection on the contaminant concentration. In regions with increased flow velocity (such as through the aperture), there is a significant decrease in water vapor concentration compared to the surrounding environment. This is another aspect that is not included in the analytical model of Scialdone, but is discussed in the work of Woronowicz. However, diffusion does play an important role in the contaminant transfer. This is mainly visible in the secondary volume. The primary flow passes over the cup, and ends up reducing the water concentration in front of the cup opening. The resulting concentration gradient then helps drive off the internal moisture from within this secondary volume.

Fluid flows can be described as laminar or turbulent, with the Reynolds number providing an indicator of the expected flow regime. For a flow in a pipe, the Reynolds number is given by $Re = uD/\nu$, where u is the flow speed, D is the pipe diameter, and $\nu = \mu/\rho$ is the kinematic viscosity. Generally, pipe flow with $Re < 2300$ is considered to be laminar, and turbulent for $Re > 4000$. Using the test pipe and aperture diameters of 0.25 and 0.01 m, respectively, we can compute the two Reynolds number to be $Re_{pipe} = 3630$ and $Re_{aperture} = 160$. In the previous calculation, flow speed was computed as $u \equiv Q/A = 0.21$m/s for $Q = 1$L/min, and $\nu = 1.46 \times 10^{-5}$m^2/s. This is in fact confirmed by the numerical simulation. A laminar flow can be seen to exist across the aperture

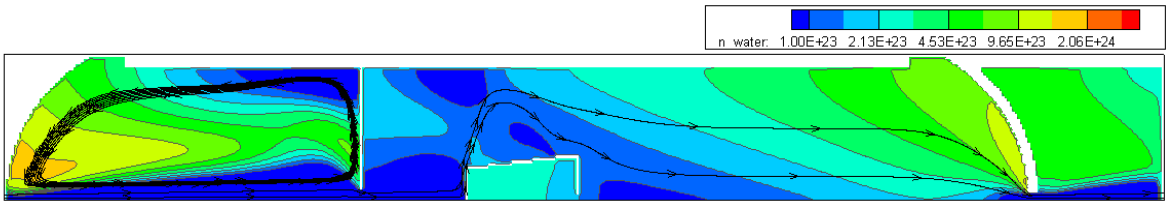

(a) water vapor density

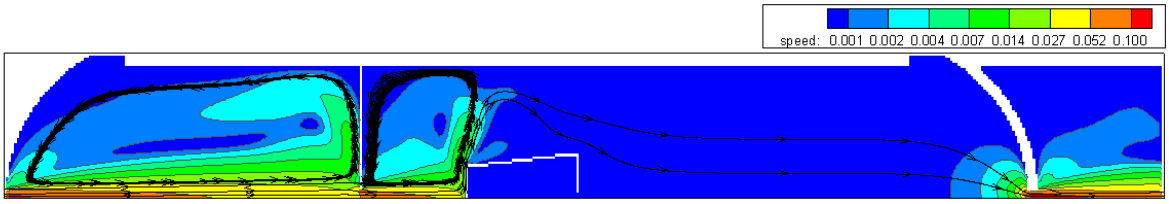

(b) flow speed

Figure 13. Preliminary purge flow simulation results. Figure (a) shows the water vapor density while (b) shows the flow speed.

and the baffle opening. However, within the cavity, several vortexes can be seen to form. This vortex formation results in some regions of the cavity being more difficult to dry off than other. The vortex formation may however be assisted by the inlet boundary condition, containing only an axial flow. As such, the solution does have some resemblance to the lid-driven cavity case often studied in fluid-dynamics. It should also be noted that the preliminary results discussed in this section were computed without including treatment for turbulent flow in the numerical code. Turbulent features can be studied using approaches such as RANS, in which the flow is split into a time-averaged value, and a random turbulent oscillation. Inclusion of the RANS model and studying the impact of the inlet boundary condition is left for future work.

5. CONCLUSION AND FUTURE WORK

In this paper we summarized an experimental and numerical effort to study the removal and infiltration of a contaminant such as water vapor into an enclosed cavity. More specifically, the results were compared against a well known analytical model of Scialdone. By purging a cylindrical cavity containing multiple internal sensors, we found that although some similarities exist between the experiment and the model, there were also several discrepancies. The primary differences existed in the rate of contaminant removal and in the steady state behavior. The analytical model predicted a faster initial dry off, but higher steady state contaminant concentration. Some of these findings can be attributed to the fact that the model is based on the assumption of the ambient contaminant diffusing into the cavity, without taking into account impact of flow velocity. By allowing the external humidity to diffuse into the cavity once the purge was stopped, we were also obtain data on a contaminant infiltration. The most interesting finding here was that the internal concentration never reached the ambient levels, but instead leveled off at values ranging from 50 to 73% of the ambient. This finding seems to indicate that the "conductance" through the aperture is not a constant value but is instead a function of the concentration gradient.

Besides providing data for the comparison with the analytical model, the experiment was also used to obtain a set of validation data for a numerical simulation. The numerical effort was based on a combined advection-diffusion and incompressible Navier-Stokes solver. Results from the simulation were presented but additional work still remains in improving the agreement. Once better agreement is achieved, we anticipate using the tool to study the purge and infiltration problem in more detail. Specifically, we will be interested in determining the temporal variation in the aperture conductance, and also will use the code to study the impact of external impingement flow on the infiltration rate. By combining the code with a particle tracing algorithm[13] we will also be able to study the impact of purge on particulate contamination, including in a complex flow field such as a spacecraft fairing.[14]

Acknowledgement

The authors would like to acknowledge Gregory Bennett (GOES-R engineering co-op) for performing initial research on pressure and humidity sensors; John Fiorello Jr. and Zoe Dormuth (GOES-R engineering interns) for supporting data collection activities; Steve McKim, Hal Baesh, and the rest of GSFC propulsion lab for making the testing possible; and Rob Studer at GOES-R, and Mark Secunda, David Hughes, Mike Woronowicz and Evelyn Lambert at NASA/GSFC contamination branch for fruitful discussions on purge testing and analysis. This effort was supported by the GOES-R and MMS projects.

REFERENCES

[1] Scialdone, J. J., "Water-vapor pressure control in a volume," in [*NASA Technical Paper 1172*], (1978).

[2] Scialdone, J. J., "Preventing molecular and particulate infiltration in a confined volume," in [*SPIE Conference on Optical System Contamination*], **3784** (1999).

[3] Woronowicz, M., "Observations on one-dimensional counterflow diffusion problem," in [*SPIE Conference on Optical System Contamination*], (2002).

[4] Author, U., "Preformance specification: propellant pressurizing agent, nitrogen," Tech. Rep. MIL-PRF-27401D (1995).

[5] "Low voltage humidity sensors." `http://sensing.honeywell.com/honeywell-sensing-hih5030-5031%20series-product-sheet-009050-2-en.pdf?name=HIH-5030-001`.

[6] "Media resistant and high temperature accuracy integrated silicon pressure sensor for measuring absolute pressure." `http://cache.freescale.com/files/sensors/doc/data_sheet/MPXHZ6130A.pdf`.

[7] "Low voltage temperature sensors." `http://www.analog.com/static/imported-files/data_sheets/TMP35_36_37.pdf`.

[8] "Vapor pressure." `http://www.srh.noaa.gov/images/epz/wxcalc/vaporPressure.pdf`.

[9] O'Hanlon, J. F., [*A user's guide to vacuum technology*], John Wiley & Sons (2005).

[10] Schwertz, F. and Brow, J. E., "Diffusivity of water vapor in some common gases," *The Journal of Chemical Physics* **19**(5), 640–646 (1951).

[11] Tanehill, J., Anderson, D. A., and Pletcher, R. H., "Computational fluid mechanics and heat transfer," *Taylor &Francis* (1997).

[12] Chorin, A. J., "On the convergence of discrete approximations to the navier-stokes equations," *Mathematics of Computation* **23**(106), 341–353 (1969).

[13] Brieda, L., Gordon, T., and Arun, S., "Analysis of molecular conductance through a labyrinth vent," in [*SPIE Optics and Photonics*], (2014).

[14] Brieda, L., Barrie, A., Hughes, D., and Errigo, T., "Analysis of particulate contamination during launch of the mms mission," in [*SPIE Optics and Photonics*], (2010).